

This is a self-archived version of an original article. This version may differ from the original in pagination and typographic details.

Author(s): Romell, Jenny; Jie, Vun Wen; Miettinen, Arttu; Baird, Emily; Hertz, Hans M.

Title: Laboratory phase-contrast nanotomography of unstained *Bombus terrestris* compound eyes

Year: 2021

Version: Published version

Copyright: © 2021 the Authors

Rights: CC BY-NC-ND 4.0

Rights url: <https://creativecommons.org/licenses/by-nc-nd/4.0/>

Please cite the original version:

Romell, J., Jie, V. W., Miettinen, A., Baird, E., & Hertz, H. M. (2021). Laboratory phase-contrast nanotomography of unstained *Bombus terrestris* compound eyes. *Journal of Microscopy*, 283(1), 29-40. <https://doi.org/10.1111/jmi.13005>

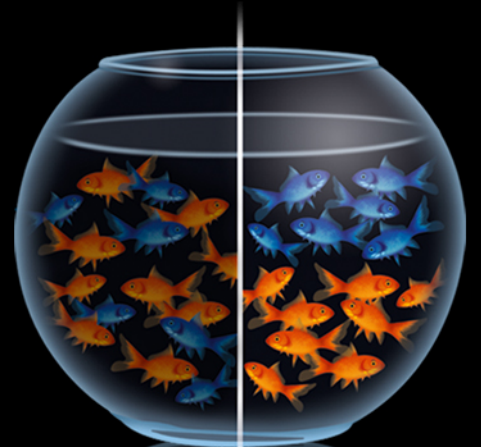
rapidFLIM^{HiRes}

Redefining standards for dynamic FLIM imaging

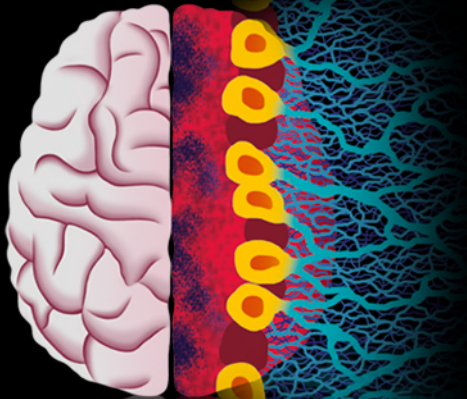


**SEE THE
CHANGE.**

**SEE IT
PRECISELY.**



**SEE IT
CONFOCAL.**



DOWNLOAD Free White Paper



PICOQUANT

Laboratory phase-contrast nanotomography of unstained *Bombus terrestris* compound eyes

Jenny Romell¹ | Vun Wen Jie² | Arttu Miettinen^{3,4,5} | Emily Baird² | Hans M. Hertz¹

¹ Department of Applied Physics, KTH Royal Institute of Technology, Stockholm, Sweden

² Department of Zoology, Stockholm University, Stockholm, Sweden

³ Institute for Biomedical Engineering, Zurich University and ETH Zurich, Zurich, Switzerland

⁴ Swiss Light Source, Paul Scherrer Institute, Villigen, Switzerland

⁵ Arttu Miettinen, Department of Physics, University of Jyväskylä, Jyväskylä, Finland

Correspondence

Jenny Romell, Department of Applied Physics, KTH Royal Institute of Technology, Stockholm, Sweden.
Email: jenny.romell@biox.kth.se

Funding information

Knut and Alice Wallenberg Foundation; Swedish Research Council, Grant 2018-06238

Abstract

Imaging the visual systems of bumblebees and other pollinating insects may increase understanding of their dependence on specific habitats and how they will be affected by climate change. Current high-resolution imaging methods are either limited to two dimensions (light- and electron microscopy) or have limited access (synchrotron radiation x-ray tomography). For x-ray imaging, heavy metal stains are often used to increase contrast. Here, we present micron-resolution imaging of compound eyes of buff-tailed bumblebees (*Bombus terrestris*) using a table-top x-ray nanotomography (nano-CT) system. By propagation-based phase-contrast imaging, the use of stains was avoided and the microanatomy could more accurately be reconstructed than in samples stained with phosphotungstic acid or osmium tetroxide. The findings in the nano-CT images of the compound eye were confirmed by comparisons with light- and transmission electron microscopy of the same sample and finally, comparisons to synchrotron radiation tomography as well as to a commercial micro-CT system were done.

KEYWORDS

bumblebee, compound eyes, laboratory nano-CT, phase contrast, system comparison

1 | INTRODUCTION

Bumblebees and other pollinating insects are crucial for maintaining biodiversity and food production, but their numbers are drastically declining across the globe,^{1,2} due to habitat destruction and climate change.^{3,4} In order to protect these pollinators, we need to get a sense of how they interact with their environment. This can be achieved, at least in part, by studying their visual systems, since the eye morphology in insects is closely linked to habitat type.⁵ To be able to forage efficiently within a specific habitat type, pollinators such as bumblebees need to navigate between

spatially distributed food sources and their nest, which requires visual guidance. Their large faceted compound eyes contain thousands of photosensitive subunits (ommatidia) that are used to control flight and to detect flowers by providing temporal, spatial and colour vision.^{6,7} A specialized region that is sensitive to polarized light, known as the dorsal rim area (DRA), plays a particularly important role in helping them to navigate between flower patches and their nest.⁸ Understanding the visual systems of bumblebees and other insects will help us to better understand how climate change will affect their foraging and pollinating abilities.

This is an open access article under the terms of the [Creative Commons Attribution-NonCommercial-NoDerivs](https://creativecommons.org/licenses/by-nc-nd/4.0/) License, which permits use and distribution in any medium, provided the original work is properly cited, the use is non-commercial and no modifications or adaptations are made.

© 2021 The Authors. *Journal of Microscopy* published by John Wiley & Sons Ltd on behalf of Royal Microscopical Society

Different imaging methods play different roles in increasing the understanding of the anatomy and ultimately function of the compound eye. Histological analysis through electron microscopy or light microscopy (LM) can provide excellent resolution in two-dimensional sections but is destructive and labour-intensive; the preparations required before viewing the sample in a microscope includes fixation, embedding, sectioning and staining. The sections are viewed one by one and the volume information is limited due to sample deformation and a finite thickness when slicing. Another difficulty is determining the orientation when slicing, to ensure that structures are not cut off obliquely, which may complicate the image interpretation.

X-ray computed tomography (CT) can instead be used to non-destructively recreate a three-dimensional image of a specimen.^{9,10} The resulting data can either be viewed as a volume or sliced in arbitrary directions to perform a virtual histological analysis. The method of acquiring x-ray projection images of a sample at different viewing angles and then creating a cross-sectional reconstruction has been used for decades¹¹ but is constantly seeing new developments in terms of contrast and resolution. Micro- and nano-CT, that is tomographic imaging with micrometre and sub-micrometre resolution, are available both in commercial laboratory systems and at large-scale synchrotron facilities (see, e.g. Refs.^{12–14}). Applications range from medicine and biology to geology and material science. Micro-CT is also a valuable tool for studying the morphology of insect brains¹⁵ and has been used to assess properties such as the visual field, resolution and optical sensitivity of the eye.^{10,16}

In conventional CT, image contrast arises from the difference in attenuation the x-rays experience as they pass through the sample. Hard and dense materials with high atomic number, such as bone and metal, show strong attenuation, while x-rays more easily penetrate materials with low atomic number. Soft biological tissues and water are difficult to image in a conventional x-ray arrangement due to their low, and very similar, x-ray attenuation coefficients. To overcome this lack of contrast, biological samples are often stained with different heavy metals, such as tungsten, lead, silver, osmium or uranium.^{17–19} Even though it is a good way to increase the image contrast, staining can have several disadvantages: (i) Heavy metals are a potential hazard, both for the scientist handling the sample, and for the environment if not disposed of correctly; (ii) If the staining solution does not penetrate the tissue uniformly, we may get images that are difficult to interpret; (iii) Introducing heavy metals into our sample may change the biological tissue under examination, and raises the question: Do we see a true representation of the sample, or artefacts from the stain?

To avoid staining biological tissues, x-ray phase-contrast imaging can be used. Instead of only detecting how much the x-rays are attenuated, a phase-sensitive imaging arrangement also measures how much the phase of the radiation is shifted when the x-rays pass through the sample. The phase shift is typically orders of magnitude stronger than absorption for light materials at hard x-ray energies, which means that we can get enhanced contrast in our images by choosing a phase-sensitive imaging arrangement rather than conventional attenuation contrast.²⁰ There are some different approaches to detecting the phase. The most widely used arrangements are grating-based imaging (GBI)^{21,22} and propagation-based imaging (PBI).²³ In GBI, the first-order spatial derivative of the phase is measured by grating interferometry. Attenuation and dark-field images can be independently reconstructed.²⁴ Grating-based imaging enables quantitative imaging of the phase, but image quality is dependent on high-quality gratings.²⁵

The PBI arrangement enables higher resolution and is simpler, as no components besides x-ray source, sample and detector are needed. The second-order derivative of the phase shift is detected by placing the camera at a distance from the sample. The propagation distance allows an interference pattern to be formed in the detector plane, caused by the small angular deviations that arise from the phase shift in the sample. Although PBI does not need any optics, the requirements on x-ray source and detector are somewhat higher. The x-ray source needs to provide radiation with enough spatial coherence to enable interference, and therefore this type of imaging has mainly been performed at synchrotron facilities.²⁶ Recent developments in electron-impact x-ray sources have enabled laboratory phase-contrast imaging using PBI, with promising results in, for example, zebrafish muscle,²⁷ mouse brain,²⁸ velvet worm myoanatomy²⁹ and mummified soft tissue.³⁰ A few cases of phase-contrast imaging of insects have been reported, but they are to date limited to fossils in amber and stained or dried specimens (see, for example, Refs.^{31,32}).

Here, we present x-ray phase-contrast imaging of the compound eyes of bumblebees, without the use of any staining agents. An in-house phase-contrast nano-CT system built with a tabletop nanofocus x-ray source has primarily been used. We describe the appearance of the compound eyes – from cornea and CC to photoreceptor cells – and compare phase-contrast nano-CT images to histology by light and electron microscopy. As an example, we also present CT imaging of the specialized DRA of the compound eye. For a comparison of x-ray CT systems, the same specimens were imaged with a commercial micro-CT machine, and finally at a synchrotron facility. Focusing on laboratory systems, we also compare samples stained with

phosphotungstic acid (PTA) and osmium tetroxide (OsO_4) to samples where no staining was used.

2 | MATERIALS AND METHODS

2.1 | Sample preparation

Buff-tailed bumblebees (*Bombus terrestris*) were dissected and compound eye samples were fixed in paraformaldehyde (3%), glutaraldehyde and glucose (2%), in a phosphate buffer for 1–3 h. One sample was then stained with osmium tetroxide (OsO_4), one with PTA and one was left unstained. A graded alcohol series was used for dehydration and finally the samples were embedded in epoxy resin (Agar 100), which was cured at 60°C for 2 days. External resin was removed and tissue surrounding the compound eye was trimmed down to minimize the sample size. The eyes were glued onto needles suitable for mounting in the sample holders of the respective systems.

2.2 | High-resolution tomographic imaging

Tomography was primarily performed using an in-house nano-CT system built upon a nanofocus x-ray source (NanoTube N1, Excillum AB).^{33,34} For comparison, the samples were also scanned with a commercial laboratory micro-CT system (Zeiss Xradia 520 Versa, Zeiss Microscopy),³⁵ and at a synchrotron facility (Swiss Light Source).³⁶ The procedure for performing a CT scan was similar across the imaging systems used in this study: the sample was put on a rotation stage, and x-ray projection images were acquired at different angles. Flat-field images, without the sample in the field-of-view, were acquired and used for correcting for inhomogeneous illumination and detector imperfections. Transverse reconstructions were created, and finally the stack of reconstructed slices was combined into a volume representing the sample.

2.2.1 | The NanoTube N1 nano-CT system

For high-resolution laboratory imaging of the compound eye, an in-house nano-CT system was used. This arrangement uses a cone-beam geometry, and is depicted in Figure 1. The system was built with a nanofocus transmission x-ray source NanoTube N1 (Excillum AB) which has a tungsten anode and gives a round x-ray emission spot with a diameter down to 300 nm. While a small spot size is necessary for high resolution, it also means lower power. The spot size should thus be chosen to the largest acceptable in order to minimize exposure times. For this

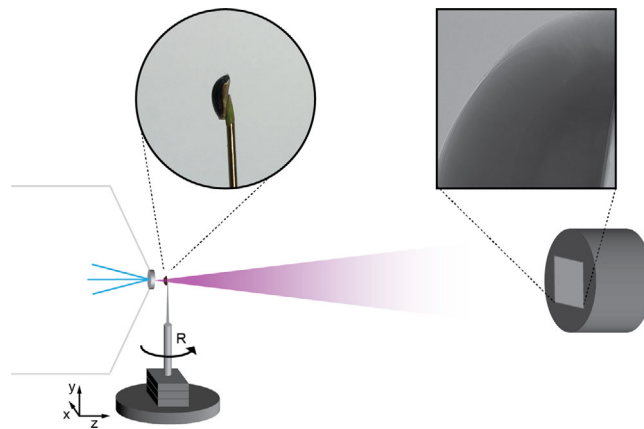


FIGURE 1 Phase-contrast imaging with the NanoTube N1 nano-CT system. The compound eye sample, glued on a needle, was placed on a rotation stage close to the x-ray source

work, acceleration voltage of 60 kV and a 500-nm spot was used. To fully utilize the resolution of the x-ray source, the imaging distances R_1 (source-to-sample distance) and R_2 (sample-to-detector distance) were chosen to give a large geometric magnification, $M_{\text{geom}} = (R_1 + R_2)/R_1$. To enhance small, low-absorbing features within the sample, we also adjust the effective propagation distance, given by $z_{\text{eff}} = R_2/M_{\text{geom}} = R_1 R_2 / (R_1 + R_2)$. With a large magnification, the propagation distance $z_{\text{eff}} \approx R_1$, which means the distance between the source and the sample, will govern the effects of the phase shift in the images. The effective propagation distance will give a maximum contrast for spatial frequency u , at a given wavelength λ according to $z_{\text{eff}} = 1/(2u^2\lambda)$.³⁷ With the distance $R_1 = 6.2$ mm and 32 \times magnification, the propagation distance $z_{\text{eff}} = 6.0$ mm was tailored for imaging micron-sized structures. A sCMOS camera (Photonic Science) with a 10- μm thick Gadox scintillator was used. The sample-plane pixel size was 280 nm and the effective field-of-view 1.1 mm. After acquisition of projection images at 2001 different angles, a short scan was performed to detect sample drift during acquisition. Further details are given in the Supplementary Materials.

2.2.2 | Zeiss Xradia 520 Versa

The Zeiss Xradia 520 Versa system offers imaging in a variety length scales and resolution. Instead of pure geometric magnification (M_{geom}), the charge-coupled device (CCD) detector comes with different objectives with magnifications $M_{\text{obj}} = 0.4, 4, 20$ or 40 \times , giving a total system magnification $M = M_{\text{geom}} \cdot M_{\text{obj}}$.

The x-ray source of the Versa system is similar to the NanoTube; it has a transmission anode made of tungsten,

and was also run at 60 kV acceleration voltage. Emission spot size is not available to adjust in the Versa system, but otherwise as many scan parameters as possible were kept comparable with the nano-CT scans. The 20× objective and shortest possible imaging distances gave a sample-plane pixel size of 370 nm, up to 760 μm field-of-view and an effective propagation distance of 5.2 mm. The exposure time for the Versa scan (7 s) was matched to give approximately the same dose as with the nano-CT system. Details of the nano-CT and Versa scanning parameters can be found in the Supplementary Materials.

2.2.3 | The TOMCAT beamline at Swiss Light Source

Fast imaging is beneficial for avoiding artefacts such as thermal drift, but is rarely possible with laboratory systems at micron resolution. At the beamline for TOMographic Microscopy and Coherent rAdiology experimentTs (TOMCAT), Swiss Light Source, the bumblebee eyes were scanned with 200-ms exposure time per projection at a beam energy of 20 keV. With a 20× objective, the pixel size was 325 nm and the field-of-view 830 μm wide. The sample–detector distance was 80 mm. Since the imaging distance was longer and the dose much higher, the resulting images from TOMCAT are not directly comparable to those of the laboratory systems, but are shown here to give a view of the gold standard method.

2.2.4 | Image processing and analysis

All projections were first flat-field corrected to account for detector imperfections and inhomogeneous x-ray illumination. For the nano-CT data, phase retrieval was performed to recover the phase information from the edge-enhanced projection images. This was done in MATLAB, based on Paganin's method.³⁸ The ratios between δ (complex refractive index decrement) and μ (attenuation coefficient) of the unstained, PTA stained and osmium stained samples were assumed to be 10^{-6} , $5 \cdot 10^{-7}$ and 10^{-7} , and the average energy 15 keV. The choice of these parameters, which decided the degree of filtering, was done by visual inspection. During phase retrieval, all projections were corrected to account for sample motion due to thermal drift. See Supplementary Materials for more details on phase retrieval and drift correction.

The Xradia 520 Versa reconstruction software does not include any phase retrieval, but directly generates a 3D volume. For a fair comparison to the in-house nano-CT system, the images of the unstained sample from the Versa system were also phase retrieved, using the same algorithm as above, but applied to the already reconstructed data.

While phase retrieval is normally performed on projection images, the order of the Paganin filter and the reconstruction filter, both applied in the Fourier domain, can be changed.³⁹ Phase retrieval of Versa data has previously been reported successful.^{40,41}

To reconstruct a 3D volume from the nano-CT projection images, a cone-beam variety of the filtered back projection (FBP) was used (Feldkamp–David–Kress, FDK).⁴² For the synchrotron data, the gridrec reconstruction algorithm was used.⁴³ The reconstructions of the compound eyes were visualized in two different ways: As volume renderings, and sliced to perform virtual histological analysis. ImageJ (National Institute of Health) and Amira Software (Thermo Fisher Scientific) were the main tools for visualization and analysis.

2.3 | Histology

For comparative histology by LM and transmission electron microscopy (TEM), the unstained sample was cut into three pieces: The dorsal part of the eye, containing the DRA, and two pieces more ventral. These three pieces were individually embedded and sliced in micron-thick sections for LM, and sections about 80 nm thick for TEM. The DRA and the neighbouring piece were sliced transversally to the photoreceptors, and the most ventral part approximately longitudinally. For LM, Toluidine blue was used as staining, and for TEM the slices were first stained with Reynold's lead citrate followed by uranyl acetate.

3 | RESULTS

3.1 | The compound eye

The in-house nano-CT system enabled imaging with 280-nm isotropic voxels in a 1.1×1.1 mm field-of-view, allowing for detailed analysis of the whole width of the compound eye. Figure 2(A) shows the sample mounted on a needle with the approximate field-of-view marked (dashed rectangle). Volume renderings from a reconstruction of the unstained compound eye are shown virtually sectioned in two different orientations. This gives an overview of the different parts of the eye: The outermost layer of corneal lenses (Co), recognized through their characteristic hexagonal pattern, focuses the incident light. The crystalline cones (CC) further focus the light into the retina (R), where it is detected by photoreceptor cells. The photoreceptor cells transmit their signals to axons through the basement membrane (BM) at the back of the eye. One photoreceptor unit (lens, CC and photoreceptor cell) is known as an ommatidium and its appearance in CT images is described

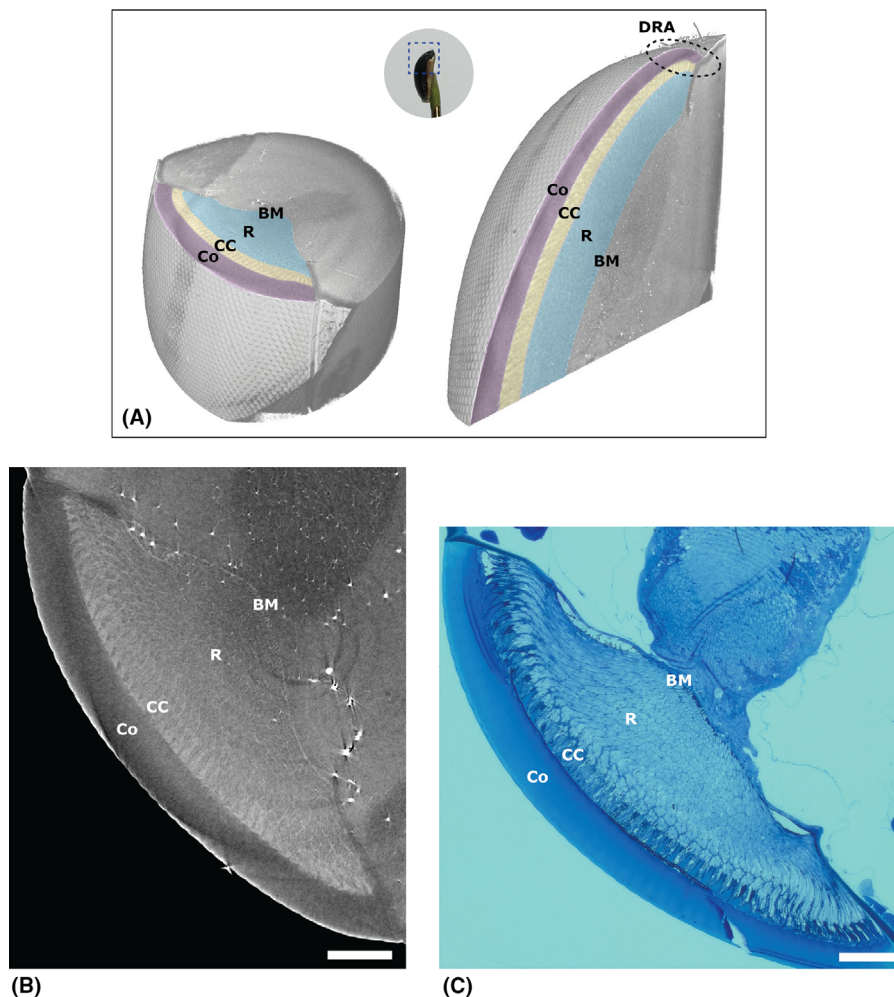


FIGURE 2 Overview of the compound eye. (A) Photo of the mounted eye indicating the field-of-view of the nano-CT scans. Volume renderings from the nano-CT scan are virtually cut in two different orientations, where cornea (Co), crystalline cones (CC), retina (R), basement membrane (BM) and the approximate position of the dorsal rim area (DRA) are marked. (B) Virtual nano-CT slice and (C) corresponding microscopy image. Scale bars: 100 μm

further below. The approximate position of the specialized DRA is also indicated. A virtual slice through the CT data is shown in Figure 2(B). Microscopic structures, such as CC and BM can be captured non-destructively in high resolution. As comparison, an LM image is shown in Figure 2(C).

3.1.1 | Ommatidia

There are thousands of ommatidia in one compound eye, with the task of focusing and detecting incident light. Figure 3(A–C) summarizes the appearance of these structures imaged with our laboratory nano-CT system. TEM images (Figure 3D–F) from the same sample are presented as reference.

When the light incident on the eye passes the corneal lens, it is focussed through a CC down to the retina (seen in longitudinal sections in Figures 3A and D, and

transversal in Figures 3B and E). To prevent the light from going through one CC into neighbouring photoreceptors, the cone is surrounded by pigment cells, with the task of absorbing any stray light. The screening pigment (P) appears brighter than the surrounding material in the phase-contrast nano-CT image, indicating higher electron density. The individual pigment granules are seen as black dots, the size of a few tens to a few hundred nanometres, in the TEM images. Figures 3(B) and (E) show transversal sections through the CC in CT and TEM, respectively. Here, the pigment is visible as a ring around the circular cross-section of the cone. Deeper into the eye, one single ommatidium consists of eight elongated photoreceptor cells, that resembles a flower pattern if sectioned transversally, as seen in Figures 3(C) and (F). The eight cells (marked by numbers 1–8) together contribute to the light-sensitive rhabdom (Rh), which consists of microvilli from these eight cells, in the centre of the ommatidium. The

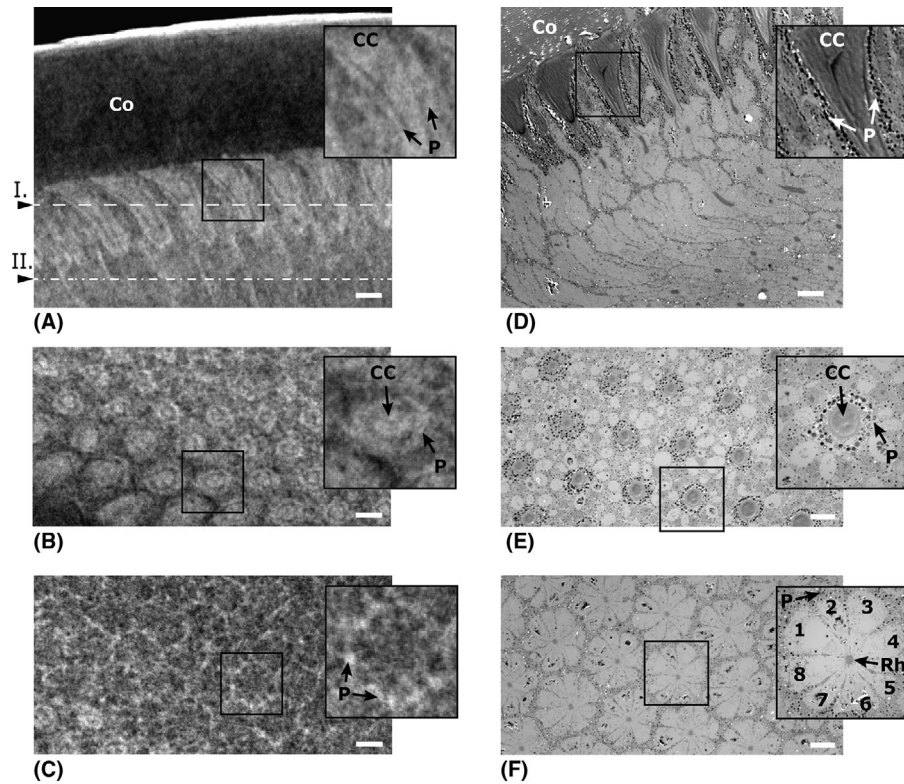


FIGURE 3 Ommatidia imaged with nano-CT (A–C, unstained) and TEM (D–F, lead citrate and uranyl acetate staining). (A) and (D) Longitudinal sections through crystalline cones (CC). Pigment (P) surrounding the cones is seen in both CT and TEM. (B) and (C) show virtual CT sections at positions I and II, respectively, and (E) and (F) are TEM sections at similar positions. The sections in (C) and (F) are taken transversally to the photoreceptor cells, showing the flower patterns formed by the eight cells of each ommatidium, here marked with numbers 1–8. The rhabdom (Rh) consists of microvilli from all eight cells. Scalebars: 10 μm

rhabdom is clearly visible in TEM images, and is shown in more detail when discussing the DRA characteristics below. With phase-contrast nano-CT, the contrast within the retina mainly arises from differences in pigmentation. The outline of the group of photoreceptor cells in each ommatidium is thus captured, as there is screening pigment also surrounding the photoreceptor cells. The individual cells are barely distinguishable since the walls separating them are thinner than what the system can resolve ($<0.5 \mu\text{m}$). The rhabdom, which is about 1–2 μm in diameter, cannot be seen in the CT images, possibly due to the weak natural contrast between the microvilli and the cell bodies, and the relatively high noise level.

3.1.2 | Dorsal rim area

The DRA, which is found on the dorsal edge of the eye as indicated by Figure 2(A), is a region of the eye containing a subset of photoreceptors that are specialized anatomically^{44,45} and physiologically^{46–48} in detecting the orientation of electric field vector distribution of skylight due to scattering by air molecules in the atmosphere.^{49,50}

The ommatidia in this area will usually appear different to those in the non-DRA regions, particularly in rhabdom shape, microvilli orientation and optics. One way to determine the presence of polarization sensitivity, particularly in insects, is by looking for the mentioned anatomical differences in rhabdom shape and microvillar orientation through transverse sections of the photoreceptors with TEM.

For *B. terrestris*, the DRA anatomical profile has not yet been well established,⁵¹ but here we can report on some differences between the DRA and the rest of the eye, found with nano-CT. The first thing to note is that the lenses, which are best visualized in a volume rendering, are almost square or irregularly shaped at the position of the DRA, and not hexagonal as in the rest of the eye (Figure 4A). Although this is not always an indication of where to find polarization sensitive ommatidia,⁵² it may roughly show the position of the DRA and thus provide guidance on where to perform a high-resolution region-of-interest CT scan or make a section for histology. Virtual sections through the CC, shown in Figures 4(B) and (C) show that the DRA cones are both thinner and shorter than the non-DRA ones, as well as more irregularly spaced.

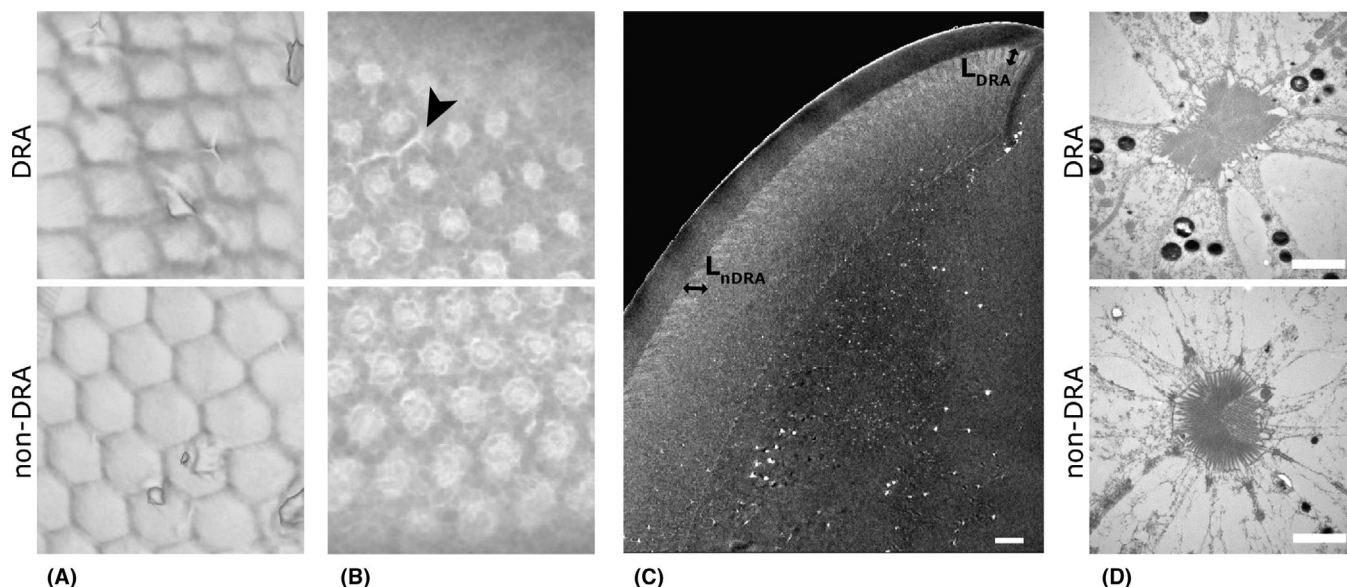


FIGURE 4 Characteristics of the DRA compared to the non-DRA: nano-CT and TEM. (A) Nano-CT volume rendering (approx. $90 \times 90 \mu\text{m}$) showing the different shape of the facets. (B) Virtual transversal section through the volume in (A), showing the cones. In the DRA, cones are smaller and irregularly spaced. Arrow marks dense structure, possibly pigment. (C) Length of the crystalline cones in the DRA (L_{DRA}) is about $30 \mu\text{m}$ while non-DRA cones are about $40 \mu\text{m}$ long (L_{nDRA}). Scalebar: $50 \mu\text{m}$. (D) TEM images of the DRA- and non-DRA rhabdoms. Scalebar: $1 \mu\text{m}$

Denser structures, which in the CT reconstruction resemble pigment, could be seen between some of the cones in the DRA (arrow in 4B). Electron microscopy of the photoreceptors, shown in Figure 4(D), confirms the difference in shape between the DRA rhabdoms (elongated rectangular) and non-DRA rhabdoms (round).

3.2 | Comparisons

The majority of the imaging in this work was done with a laboratory nano-CT system but comparative measurements were also done with the commercially available Xradia 520 Versa micro-CT system and at the TOMCAT beamline at the Swiss Light Source. Virtual sections through the unstained compound eye imaged with all three systems are shown in Figure 5. The sections are taken at approximately the same position in all data sets, and give an oblique view through the cornea, CC and photoreceptors. Cones and photoreceptors are shown in detail in the enlarged view of the marked regions (dashed and solid rectangles, respectively). With the nano-CT system (Figure 5A), the outline of the groups of photoreceptor cells can be seen, and cones and pigment cells can be distinguished (see also Figures 3B and C). The Versa system (Figure 5B) does not manage to capture much of the details of the eye structure using their standard reconstruction software, which is made for attenuation-based micro-CT. Vague outlines of the photoreceptor cells and the cones can be seen, but the attenua-

tion in these structures is very low and signal-to-noise ratio not high enough for any further analysis. If a Paganin filter is applied after reconstruction, more details appear (Figure 5C). The shape of photoreceptor groups can be seen, and also the CC. There is no distinction between the cones and the surrounding pigment here, due to the low spatial resolution. In Figure 5(D), synchrotron radiation CT of the same sample is shown. Here, the photoreceptors and cones with pigments are clearly identifiable. Note that the imaging geometry and dose for this scan was different, and that no phase retrieval filter was applied.

Samples stained with osmium and PTA were imaged using the same settings as for the unstained samples on each of the laboratory systems. These results are summarized in Figure 6; osmium in the left column and PTA in the right. For the nano-CT scan (Figure 6A-B) a very modest phase retrieval filter was applied while the Versa images (Figure 6C-D) were produced using the standard reconstruction. Osmium appears to target the cones and retina, while PTA gives a somewhat increased contrast for the cones. In the nano-CT reconstructions, fewer details are seen in the stained samples than in the unstained. The image quality for both osmium and PTA stained eyes are comparable between the nano-CT and Versa systems, however the Versa images show fewer artefacts. While not useful when imaging with the phase-contrast nano-CT system, staining greatly increases the quality of the images that can be produced by the Versa system, if only using their built-in software.

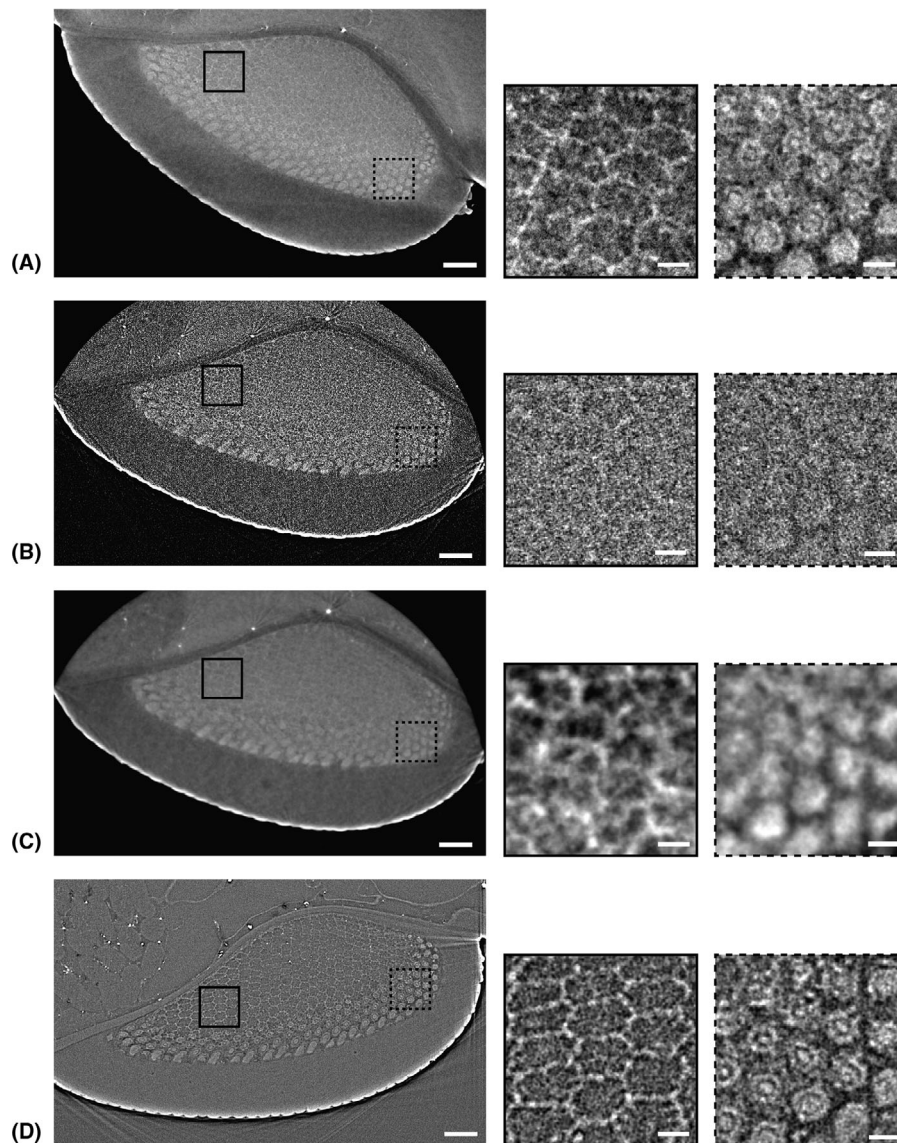


FIGURE 5 Unstained eye imaged with the three different systems. (A) NanoTube N1 nano-CT system. (B) Xradia 520 Versa (standard reconstruction). (C) Xradia 520 Versa (reconstruction with phase retrieval). (D) Synchrotron radiation tomography at the TOMCAT beamline, Swiss Light Source. Scalebars represent $50\ \mu\text{m}$ in the main figures and $10\ \mu\text{m}$ in zoomed in views

It should be noted that the Versa field-of-view at comparable voxel sizes is much smaller than that of the nano-CT system (about $700\ \mu\text{m}$ compared to $1.1\ \text{mm}$). The black, circular border in the images from the Versa system is due to limitations in the field-of-view. For a full reconstruction of the sample, the Versa software offers a wide-field mode, where two scans are performed and the projection images are stitched together before reconstruction. This mode was not used here since the whole eye just fit into the field-of-view, but must be used when scanning larger samples. If running two scans to cover the field-of-view is not an alternative, the optical magnification can be decreased, with the risk of sacrificing resolution.

4 | DISCUSSION

High-resolution 3D imaging in a laboratory setting enables virtual histological analysis of biological specimens and provides an alternative or complement to classical histology and synchrotron radiation tomography. We have shown that the photoreceptors of buff-tailed bumblebees (*B. terrestris*) can be imaged with laboratory phase-contrast nano-CT, with resolution close to $1\ \mu\text{m}$ in a 1-mm sample. We also showed that this imaging is preferably done without using any x-ray staining agents. Furthermore, we present details of the DRA of *B. terrestris* and compare the findings in nano-CT with conventional histological

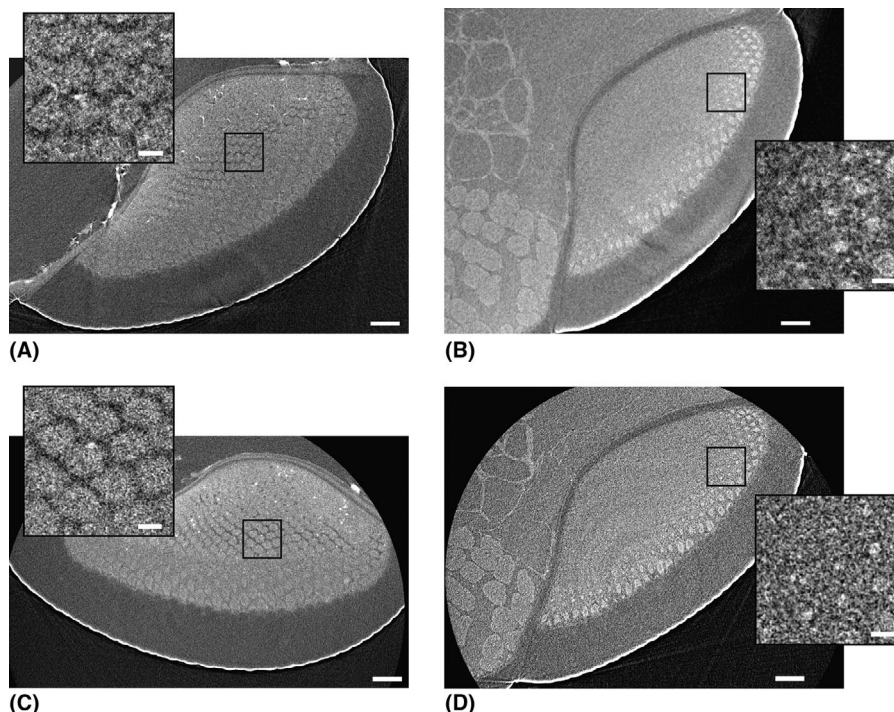


FIGURE 6 Stained compound eye samples imaged with the two laboratory systems. Left column: OsO_4 staining. Right column: PTA staining. (A–B) NanoTube N1 nano-CT system. (C–D) Xradia 520 Versa (standard reconstruction)

methods, using light- and electron microscopy, as well as with the gold standard CT available at synchrotron facilities. Finally, we compare our in-house phase-contrast nano-CT system with a commercial x-ray system, imaging samples with and without x-ray stains.

Imaging biological samples without using any x-ray staining is beneficial for several reasons. The sample is closer to its natural state, which means that we are more likely to image actual biological features and not artefacts caused by the stain. Introducing heavy metals into biological tissues is an invasive process with known adverse effects. As can be seen when comparing images of the unstained sample with the stained ones, microscopic structures are more accurately represented if staining is omitted. The sample preparations before scanning the specimen can thus be faster, since there is no need to wait for a staining agent to penetrate the tissue. Avoiding heavy metal stains, such as osmium, also reduces the risk for the scientist. Omitting the staining is one step towards imaging samples in their natural state, but there are several additional improvements to be made. Using laboratory systems, it is still necessary to use fixation and embedding due to the long exposure times, as any small deformation of the sample during the scan will impair image contrast. Developments of x-ray sources, as will be further discussed below, can give reduced scan times and will be another step towards completely non-invasive scanning.

The use of phase contrast in CT is what enables imaging of very weakly attenuating materials. The microstructures in the compound eye absorb too little of the incident x-rays to give rise to much contrast in conventional micro-CT, but more details can be depicted using phase contrast. We have shown that phase-contrast nano-CT of the compound eye acquired with a laboratory system gives comparable image quality to synchrotron radiation tomography as well as LM. The comparison of phase-contrast CT images to TEM of the same sample gives insights into which parts of the eye contributes the most to the phase signal; in particular, it seems that the CC and the pigment has higher electron density than their surroundings. The central rhabdom, on the other hand, did not appear in any of the CT scans performed in this work, probably because of lack of contrast rather than resolution (diameter is about $1.5 \mu\text{m}$ according to TEM images). If the contrast between the rhabdom and the rest of the photoreceptor cells is too weak, the signal would be drowned in the relatively high noise that is a result from using a nanofocus x-ray source – to gain resolution, x-ray flux is sacrificed due to the need for a small emission spot. Increasing the exposure, and thus scan time, is not desirable as there are also artefacts from sample drift. Higher x-ray source power is the preferred solution, and this is indeed possible with newer versions of the NanoTube, which will be discussed further below.

Scanning unstained specimens may not work on all systems. Comparing the phase-contrast nano-CT system with the Zeiss Xradia 520 Versa, it is clear that the Versa system does not give a satisfying reconstruction of the photoreceptors when imaging under the same dose as with the nano-CT system. This may have several reasons. First, the emission spot of the x-ray tube, although not reported explicitly by the Versa software, is most likely larger. This will limit the resolution and may also have an impact of the spatial coherence of the x-rays, which is crucial to be able to properly reconstruct the phase. Secondly, there is no built-in phase retrieval algorithm in the reconstruction software, as has previously been noted by others.^{40,41} By applying a Paganin filter after the reconstruction, we can more fairly compare the systems. It is clear that resolution in the Versa system is much lower, which again most likely is due to a large x-ray source emission spot. The detector scintillator is also unknown, both what material it consists of and its thickness, and this will also affect what resolution the system can ultimately achieve. However, even with lower resolution than comparable nanofocus systems, implementation of a simple phase retrieval algorithm such as the Paganin filter would greatly enhance the imaging performance of the Versa system for weakly attenuating samples.

In the samples stained with PTA or OsO₄, the contrast primarily arises from attenuation instead of phase shift. Details within the compound eyes are not properly captured by any of the systems, and it is difficult to say whether that is due to lack of contrast or if the microscopic structures within the eyes have been negatively affected by the stains. What is clear here, is that the difference in quality between the nano-CT and the Versa images is much less apparent. Roughly the same structures can be seen, and here the Versa gives a cleaner reconstruction, probably due to shorter exposure times and thus less sample drift. Even though our nano-CT system outperforms Versa in phase-contrast imaging and resolution, the overall image quality for attenuation-based images is comparable between the two systems. Exposure times for the nano-CT were however much longer. This first nano-CT system was built with a NanoTube N1, which is one of the early models of the NanoTube. The currently available model, NanoTube N2, offers three times higher power at the same emission spot size, which means that future NanoTube-based systems can perform the same kind of imaging as presented here, in just a third of the time. This means exposure times in the same range as, or even shorter than the Versa system. A reduction of exposure time enables higher throughput as well as improving the image quality, as the artefacts currently present in the nano-CT reconstructions mainly arise from sample drift over time. The simple drift correction method used here should also be further developed, as it does not completely remove the motion artefacts for these

samples. Other improvements to the imaging arrangement include upgrading the rotation stage and to better control the temperature in the sample environment, and will allow for sub-micron 3D resolution in unstained biological samples.

To summarize, we have shown that laboratory nano-CT using phase contrast enables virtual histology of compound eyes, and demonstrated its potential by imaging individual ommatidia and characteristics of the specialized DRA. Images comparable to both LM and synchrotron radiation tomography were captured using a laboratory system, without the need for any sectioning, staining or applying for beamtime at large-scale facilities. Laboratory phase-contrast CT thus opens up for either completely non-destructive imaging of unstained tissue at resolution around 1 micron, or multimodal imaging in combination with TEM at specific sections pinpointed in

a CT volume. This increases the number of imaging methods available and may provide new standards of how we analyse the visual systems of insects, and other biological specimens.

ACKNOWLEDGEMENTS

We acknowledge the generous funding of the Knut and Alice Wallenberg foundation. This project was supported in part by the Swedish Research Council grant 2018-06238 to EB. We also acknowledge the Paul Scherrer Institut, Villigen, Switzerland for provision of synchrotron radiation beamtime (proposal number: 20190641, to EB) at the TOM-CAT beamline X02DA of the SLS. Data acquisition at the Xradia 520 Versa system was supported by a grant to the Stockholm University Brain Imaging Centre (SU FV-5.1.2-1035-15). A special thanks to Lars Haag and Ewa Idsund-Jonsson at the Electron Microscopy Unit, Karolinska Institute, for acquisition of LM and TEM images.

CONFLICT OF INTEREST

JR, VWJ, AM and EB report no conflicts of interest. HMH is a shareholder in Excillum AB.

REFERENCES

1. Memmott, J., Waser, N. M., & Price, M. V. (2004). Tolerance of pollination networks to species extinctions. *Proceedings of the Royal Society of London, Series B: Biological Sciences*, 271(1557), 2605–2611.
2. Goulson, D. (2003). Conserving wild bees for crop pollination. *International Journal of Food Agriculture and the Environment*, 1, 142–144.
3. Winfree, R., Aguilar, R., Vázquez, D. P., LeBuhn, G., & Aizen, M. A. (2009). A meta-analysis of bees' responses to anthropogenic disturbance. *Ecology*, 90(8), 2068–2076.
4. Marshman, J., Blay-Palmer, A., & Landman, K. (2019). Anthropocene crisis: Climate change, pollinators, and food security. *Environments*, 6(2), 22.

5. Scales, J., & Butler, M. (2015). The relationship between microhabitat use, allometry, and functional variation in the eyes of Hawaiian Megalagrion damselflies. *Functional Ecology*, *30*, 356–368.
6. Linander, N., Dacke, M., & Baird, E. (2015). Bumblebees measure optic flow for position and speed control flexibly within the frontal visual field. *Journal of Experimental Biology*, *218*, 1051–1059.
7. Bernard, G., & Stavenga, D. (1978). Spectral sensitivities of retinal cells measured in intact, living bumblebees by an optical method. *Naturwissenschaften*, *65*, 442–443.
8. Wellington, W. G. (1974). Bumblebee ocelli and navigation at dusk. *Science*, *183*(4124), 550–551.
9. Baird, E., & Taylor, G. (2017). X-ray micro computed-tomography. *Current Biology*, *27*, R289–R291.
10. Taylor, G., Tichit, P., Schmidt, M., Bodey, A., Rau, C., & Baird, E. (2019). Bumblebee visual allometry results in locally improved resolution and globally improved sensitivity. *eLife*, *8*, e40613.
11. Hounsfield, G. N. (1973). Computerized transverse axial scanning (tomography): Part I. Description of system. *British Journal of Radiology*, *46*, 1016–1022.
12. ID16A – Nano-Imaging Beamline. <https://www.esrf.eu/UsersAndScience/Experiments/ID16A>
13. Zeiss Xradia 810 Ultra: Synchrotron-quality Nanoscale 3D X-ray Imaging. <https://www.zeiss.com/microscopy/int/products/x-ray-microscopy/xradia-810-ultra.html>
14. SKYSCAN 2214: 3D X-ray Microscopy at the Nanoscale. <https://www.bruker.com/en/products-and-solutions/microscopes/3d-x-ray-microscopes/skyscan-2214.html>
15. Ribí, W., Senden, T., Sakellariou, A., Limaye, A., & Zhang, S. (2008). Imaging honey bee brain anatomy with micro-x-ray-computed tomography. *Journal of Neuroscience Methods*, *171*, 93–97.
16. Taylor, G. J., Hall, S. A., Gren, J. A., & Baird, E. (2020). Exploring the visual world of fossilized and modern fungus gnat eyes (diptera: Keroplatidae) with x-ray microtomography. *Journal of the Royal Society Interface*, *17*(163), 20190750.
17. Müller, M., Kimm, M., Ferstl, S., Allner, S., Achterhold, K., Herzen, J., Pfeiffer, F., & Busse, M. (2018). Nucleus-specific x-ray stain for 3d virtual histology. *Scientific Reports*, *8*, 17855.
18. Mizutani, R., Takeuchi, A., Hara, T., Uesugi, K., & Suzuki, Y. (2007). Computed tomography imaging of the neuronal structure of *Drosophila* brain. *Journal of Synchrotron Radiation*, *14*(3), 282–287.
19. Nomaki, H., Toyofuku, T., Tsuchiya, M., Matsuzaki, T., Uematsu, K., & Tame, A. (2015). Three-dimensional observation of foraminiferal cytoplasmic morphology and internal structures using uranium–osmium staining and micro-x-ray computed tomography. *Marine Micropaleontology*, *121*, 32–40.
20. Bravin, A., Coan, P., & Suortti, P. (2012). X-ray phase-contrast imaging: From pre-clinical applications towards clinics. *Physics in Medicine and Biology*, *58*(1), R1–R35.
21. Momose, A., Kawamoto, S., Koyama, I., Hamaishi, Y., Takai, K., & Suzuki, Y. (2003). Demonstration of X-ray Talbot interferometry. *Japanese Journal of Applied Physics*, *42*(Part 2, No. 7B), L866–L868.
22. Pfeiffer, F., Weitkamp, T., Bunk, O., & David, C. (2006). Phase retrieval and differential phase-contrast imaging with low-brilliance x-ray sources. *Nature Physics*, *2*, 258–261.
23. Snigirev, A., Snigireva, I., Kohn, V., Kuznetsov, S., & Schelokov, I. (1995). On the possibilities of x-ray phase contrast microimaging by coherent high-energy synchrotron radiation. *Review of Scientific Instruments*, *66*(12), 5486–5492.
24. Pfeiffer, F., Bech, M., Bunk, O., Kraft, P., Eikenberry, E., Brönnimann, C., Grünzweig, C., & David, C. (2008). Hard-x-ray dark-field imaging using a grating interferometer. *Nature Materials*, *7*, 134–137.
25. Thuering, T., & Stampanoni, M. (2014). Performance and optimization of x-ray grating interferometry. *Philosophical Transactions. Series A, Mathematical, Physical, and Engineering Sciences*, *372*(2010), 20130027.
26. Tuohimaa, T., Otendal, M., & Hertz, H. M. (2007). Phase-contrast x-ray imaging with a liquid-metal-jet-anode microfocus source. *Applied Physics Letters*, *91*(7), 074104.
27. Vågberg, W., Larsson, D. H., Li, M., Arner, A., & Hertz, H. M. (2015). X-ray phase-contrast tomography for high-spatial-resolution zebrafish muscle imaging. *Scientific Reports*, *5*, 16625.
28. Töpferwien, M., Krenkel, M., Vincenz, D., Stöber, F., Oelschlegel, A. M., Goldschmidt, J., & Salditt, T. (2017). Three-dimensional mouse brain cytoarchitecture revealed by laboratory-based x-ray phase-contrast tomography. *Scientific Reports*, *7*, 42847.
29. Müller, M., de Sena Oliveira, I., Allner, S., Ferstl, S., Bidola, P., Mechlem, K., Fehring, A., Hehn, L., Dierolf, M., Achterhold, K., Gleich, B., Hammel, J. U., Jahn, H., Mayer, G., & Pfeiffer, F. (2017). Myoanatomy of the velvet worm leg revealed by laboratory-based nanofocus x-ray source tomography. *Proceedings of the National Academy of Sciences*, *114*(47), 12378–12383.
30. Romell, J., Vågberg, W., Romell, M., Häggman, S., Ikram, S., & Hertz, H. M. (2018). Soft-tissue imaging in a human mummy: Propagation-based phase-contrast CT. *Radiology*, *289*(3), 670–676.
31. Tafforeau, P., Boistel, R., Boller, E., Bravin, A., Brunet, M., Chaimanee, Y., Cloetens, P., Feist, M., Hoszowska, J., Jean-Jacques, J., Kay, R., Lazzari, V., Nel, A., Nemoz, C., Thibault, X., Vignaud, P., & Zabler, S. (2006). Applications of x-ray synchrotron microtomography for non-destructive 3D studies of paleontological specimens. *Applied Physics A*, *83*, 195–202.
32. Alba-Tercedor, J. (2016). Microtomographic study on the anatomy of adult male eyes of two mayfly species. *Zoosymposia*, *11*, 101–120.
33. NanoTube N1 60 kV: Uncompromising Nano Performance. https://www.excillum.com/wp-content/uploads/2018/07/NanoTube_N1_60_kV_2017-06-12.pdf
34. Romell, J., Häggmark, I., Twengström, W., Romell, M., Häggman, S., Ikram, S., & Hertz, H. M. (2019). Virtual histology of dried and mummified biological samples by laboratory phase-contrast tomography. In *X-Ray Nanoimaging: Instruments and Methods IV*, vol. 11112 (pp. 103–110). International Society for Optics and Photonics.
35. ZEISS Xradia 520 Versa Submicron X-ray Imaging: Extending the limits of your exploration. <https://www.zeiss.com/content/dam/Microscopy/us/download/pdf/Products/xradia520versa/xradia-520-versa-product-information.pdf>
36. TOMCAT - X02DA: Tomographic Microscopy. <https://www.psi.ch/en/sls/tomcat>
37. Mayo, S. C., Miller, P. R., Wilkins, S. W., Davis, T. J., Gao, D., Gureyev, T. E., Paganin, D., Parry, D. J., Pogony, A., & Stevenson,

- A. W. (2002). Quantitative x-ray projection microscopy: Phase-contrast and multi-spectral imaging. *Journal of Microscopy*, 207(2), 79–96.
38. Paganin, D., Mayo, S. C., Gureyev, T. E., Miller, P. R., & Wilkins, S. W. (2002). Simultaneous phase and amplitude extraction from a single defocused image of a homogeneous object. *Journal of Microscopy*, 206(1), 33–40.
39. Ruhlandt, A., & Salditt, T. (2016). Three-dimensional propagation in near-field tomographic x-ray phase retrieval. *Acta Crystallographica Section A Foundations and Advances*, 72, 215–221.
40. Bidola, P., Morgan, K., Willner, M., Fehringer, A., Allner, S., Prade, F., Pfeiffer, F., & Achterhold, K. (2017). Application of sensitive, high-resolution imaging at a commercial lab-based x-ray micro-CT system using propagation-based phase retrieval. *Journal of Microscopy*, 266(2), 211–220.
41. Zeller-Plumhoff, B., Mead, J. L., Tan, D., Roose, T., Clough, G. F., Boardman, R. P., & Schneider, P. (2017). Soft tissue 3D imaging in the lab through optimised propagation-based phase contrast computed tomography. *Optics Express*, 25(26), 33451–33468.
42. Feldkamp, L. A., Davis, L. C., & Kress, J. W. (1984). Practical cone-beam algorithm. *Journal of the Optical Society of America A*, 1(6), 612–619.
43. Marone, F., & Stampanoni, M. (2012). Regridding reconstruction algorithm for real-time tomographic imaging. *Journal of Synchrotron Radiation*, 19, 1029–1037.
44. Wehner, R., Bernard, G., & Geiger, E. (1975). Twisted and non-twisted rhabdoms and their significance for polarization detection in the bee. *Journal of Comparative Physiology*, 104, 225–245.
45. Schinz, R. (1975). Structural specialization in the dorsal retina of the bee, *Apis mellifera*. *Cell and Tissue Research*, 162(1), 23–34.
46. Labhart, T. (1980). Specialized photoreceptors at the dorsal rim of the honeybee's compound eye: Polarizational and angular sensitivity. *Journal of Comparative Physiology*, 141, 19–30.
47. Labhart, T. (1986). The electrophysiology of photoreceptors in different eye regions of the desert ant, *cataglyphis bicolor*. *Journal of Comparative Physiology A*, 158, 1–7.
48. Wehner, R. (1982). *Himmelsnavigation bei Insekten: Neurophysiologie und Verhalten*. (Vierteljahrsschrift der Naturforschenden Gesellschaft in Zürich. [Beil.:] Neujahrsblatt hrsg. von d. Naturforschenden Ges. in Zürich). Orell Füssli.
49. Strutt, H. J. W. (1871). XV. On the light from the sky, its polarization and colour. *London, Edinburgh, and Dublin Philosophical Magazine and Journal of Science*, 41(271), 107–120.
50. Wehner, R. (1997). The ant's celestial compass system: spectral and polarization channels. In *Orientation and communication in arthropods* (pp. 145–185). Birkhäuser, Basel.
51. Zeil, J., Ribl, W., & Narendra, A. (2014). Polarisation vision in ants, bees and wasps. In *Polarized light and polarization vision in animal sciences* (pp. 41–60). Springer: Berlin, Heidelberg.
52. Labhart, T., & Meyer, E. P. (1999). Detectors for polarized skylight in insects: A survey of ommatidial specializations in the dorsal rim area of the compound eye. *Microscopy Research and Technique*, 47(6), 368–379.

SUPPORTING INFORMATION

Additional supporting information may be found online in the Supporting Information section at the end of the article.

How to cite this article: Romell J, Jie V, Miettinen A, et al. Laboratory phase-contrast nanotomography of unstained *Bombus terrestris* compound eyes. *Journal of Microscopy*. 2021;283:29–40. <https://doi.org/10.1111/jmi.13005>